EXTENDED SOURCE GEOMETRIES FOR MULTIPHOTON MICROSCOPY: REMOVING THE SCATTERING AMBIGUITY

by

John Caleb Speirs

A thesis submitted to the Faculty and the Board of Trustees of the Colorado School of Mines in partial fulfillment of the requirements for the degree of Master of Science (Applied Physics).

Golden, Colorado

Date _____

Signed: _____
John Caleb Speirs

Signed: _____
Dr. Jeff Squier
Thesis Advisor

Golden, Colorado

Date _____

Signed: _____
Dr. Tom Furtak
Professor and Head
Department of Engineering Physics

ABSTRACT

Presented within is a recent, speed-increasing innovation in fluorescence microscopy applied to a two-photon fluorescence microscope. The innovation of the laser, detection devices such as the charge coupled device and photo-diodes, and the theory and practice of digital processing has led to increased ability to image within scattering samples with a high degree of resolution ($\sim$1 micron for most systems) and with video frame rates (30 frames/sec or above). Laser scanning microscopes are so named because of the necessity to scan the focus of a laser beam through a sample (or to scan the sample through the focus) to form an image. In a line scanning geometry, the laser is focused via a cylindrical lens to a line which allows decreased scan time. This introduces the problem of having to use multi-element detectors which are susceptible to increased background due to cross-talk between elements. SPatIal Frequency-modulated Imaging, or SPIFI, is a method which allows the line focus geometry to image with a single element detector such as a photo-diode or a PMT by using frequency modulation along the extent of the line cursor. This method can be applied to two-photon fluorescence microscopy. Because the frequency modulation is longer than the lifetime of common fluorophores, the fluorescence follows the modulation of the illumination beam. This work will demonstrate use of SPIFI with a two-photon fluorescence microscope and characterize such a microscope.

TABLE OF CONTENTS

LIST OF FIGURES AND TABLES

ACKNOWLEDGMENTS

This thesis would not have been possible if it weren't for the motivating personality of Dr. Jeff Squier, and the mentorship of and constant help from Eric Chandler and Michael D. Young. I would like to recognize these people and thank them for their kindness to me throughout this program.

For my dear friend, Ann Marie McCall

CHAPTER 1
INTRODUCTION AND BACKGROUND

The work detailed in this thesis is a synthesis of recent innovations in imaging methods with the aim of improving the speed of image acquisition. The field of microscopy is a blossoming field with many major advances in the last 50 years. The innovation of the laser, detection devices such as the charge coupled device and photodiodes, and the theory and practice of digital processing has led to increased ability to image within scattering samples with a high degree of resolution ($\sim$1 μm for most systems) and with video frame rates (30 frames/sec or above) [1,2, 3]. Examples of three dimensional imaging have also been shown [4, 5]. The advances in laser microscopy yield applications not only to biological [2, 6] and materials science [7, 8], but to advances in microfluidics [9], microcircuits, and micro-machining [10, 11].

1.1 History of Microscopy

It is worthwhile to step back to the beginning to understand the development of the microscope. Doing so allows a better understanding of the current problems faced in modern microscopy.

Lipson, Lipson and Lipson report single lenses being in use "from time immemorial" [12]. The ancient Egyptians and Mesopotamians had used single lenses as magnifiers or "burning glasses"; the oldest surviving lens is the Nimrud lens which dates back to 700 B.C. [13] In 1270 AD Italy, the first practical optical instrument appeared: spectacles. These consisted of two single lenses side-by-side and didn't necessarily represent an improvement in optics per se but more in the application of a lenses ability to magnify [14]. It wasn't until almost 300 years later in 1590, however, that Dutchmen Hans and Zacharias Janssen introduce a two-element optical system, the compound microscope. This was simply a tube with a lens at each end, and boasted

magnifications of 3X to 9X [15]. Perhaps influenced by the compound microscope [14], perhaps just coincidentally, Leppershey produced a telescope in 1608 from the realization that two lenses, an objective and a eye lens, could produce an enlarged image of a distant object [12]; Galileo seized upon the idea and made his own to study the stars and in 1610, he published *Siderius Nuncius*, *The Starry Messenger*, a collection of his observations of the Moon, stars and, notably, the moons of Jupiter [12]. Lippershey would go on to invent binoculars [14]. These breakthroughs in optical instruments ushered in new focus on the subject of optics and the applications of the phenomena produced by light traveling through lenses.

The microscope of the Janssens would gain popularity through Hooke and Leeuwenhoek, contemporaries who improved on the idea of the microscope and made extensive use of it in biological imaging. Hooke's *Micrographia* (1665) contains detailed drawings and observations of objects ranging from a needle's point to a dust mite, and contains the first use of the word "cell" to describe features of plant tissue in cork [16]. Leeuwenhoek's microscopes were the best for that time period and only contained one lens [15]. Being inspired by *Micrographia*, he was the first to describe protozoans (from his observations of droplets of pond water) and bacteria (observed in teeth scrapings). His discoveries also helped prove the theory of blood circulation [15]. The microscope has been used in biological imaging ever since.

Improvements in optical instruments were mainly centered around better materials and better lens crafting techniques [12] until Abbe's wave interpretation of image formation in 1873 [14]. Notable advances in optics in the time between include serious studies of refraction by Snell in 1921, Newton's imaging equation (in 1670), which related the focal length of a lens to the distance between it and the object and image planes, the achromat by Hall in 1733, Fraunhofer's improved achromats and characterization of the dispersive properties of different compositions of glass in 1809 [14].

The development of theory surrounding optical phenomena didn't lead to a drastic improvement in optical instrument design until Abbe. However, several components of modern day microscopes were initially developed during this time period, including the idea of resolution as a quantity, the discovery and use of prisms and spectra, and diffraction.

Abbe's diffraction-limited resolution limit caused a shift from materials based improvements to new methods of imaging. This led to the utilization of different wavelengths of light as illumination sources (notably, UV rays by Zeiss in 1904 and X-ray imaging which, because of lack of lens material for which the index of refraction is far enough away from unity to do anything observable, is mostly used in crystallography, which utilizes the diffraction effects produced in crystals [12]). In 1952, G. Toraldo di Francia showed that by masking an aperture one could produce any resolution desired but stripping the image of intensity; this led to the development of the near-field optical microscope. Zernike's phase-contrast microscope in 1953 allowed in vivo biological observation, eliminated the need for staining and was the first to utilize spatial filtering [12].

1.2 Modern Microscopy

This section details the history of modern microscopy.

1.2.1 Confocal Microscopy

In 1961, Minsky patented a "Microscopy Apparatus" that consisted of pinholes used to reject out-of-focus scattering [17]. While not yet utilizing a laser as an illumination source, this was the beginning of confocal microscopy and enabled optical section of microscope samples [18]. It revolutionized the field of microscopy [19]. Figure 1.1 shows the capability of pinholes to section samples.

Minsky's design envisioned stage scanning, or scanning the sample through the illumination beam [17]. Others used a Nipkow disk [20], or metal disk with holes

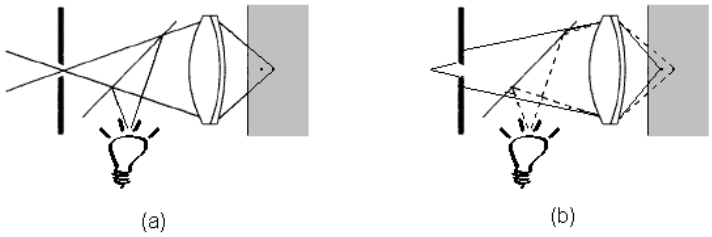

Figure 1.1: (a) Confocal microscope with all of the light from the focal plane being passed through the pinhole. (b) Out-of-focus light being rejected by the pinhole, allowing significantly less out-of-focal light through to the detector. Illumination light (and focus) is shown in a dashed line.

punched in a spiral pattern, for a scanning method. This disk, as a side note, was a central component of the first television cameras; combined with photosensitive selenium, it formed a television scanning camera which analyzed and transmitted small portions of the image at a time (the portion which the hole makes visible).

1.2.2 Laser Scanning Microscopy

Lasers have greatly influenced microscopy techniques and the decade of the 1960's saw a plethora of advances essential to modern day confocal and multiphoton microscopy. In 1938, Zernike developed and quantified the idea of coherence, and in 1960, following the invention of MASER's, Maiman invented the laser as a highly coherent light source with power densities greatly surpassing Planck's quantum thermodynamical limitation on the brightness of a light source [12]. P. Davidovits and M. D. Egger [21, 22] were the first to apply a laser light source to the confocal microscope developed by Minsky. They used a continuous wave, 5-mW He-Ne laser, noting that resolution could be improved with shorter wavelength lasers and that pulsed lasers could be used to lessen the effects of heat damage done in samples if required. Davidovits and Egger also incorporated a lens scanning method in which the objective lens was mechanically moved in order to produce the two dimensional scanning. The key ingredient was the improved illumination source. They report that in microscopy prior, "as little as 10^{-7} of the light incident from the source travels to the eyepiece to

form an image." Using a laser source allowed an image of much improved intensity to be formed.

1.2.3 Nonlinear Microscopy

It is common to use auto-fluorescence and extrinsic fluorophores in biological samples as an aid in imaging. Fluorescent markers that absorb and emit in the visible range were utilized in scanning confocal microscopes; this is known as single-photon fluorescence as one photon excites the fluorophore, and one photon of a different wavelength is emitted. Markers that absorb UV were not able to be utilized due lack of lens materials that transmit in both the wavelength of the UV excitation and the fluorescent emission without significant aberration and due to the damage UV rays would cause to biological samples [23]. It is possible for two photons of a lower wavelength (in the IR or near IR range) to excite a single fluorophore that normally absorbs a single photon in the UV range and to emit the same fluorescence that it normally would if a UV ray had excited it [23, 24], provided that they are absorbed at this same time. This process is called two-photon excitation fluorescence (TPEF), and is a nonlinear process because the intensity varies with the square of the illumination intensity. In order for TPEF to occur, an illumination pulse of sufficient intensity and small spatial extent is needed; this pulse is provided by ultra-fast pulsed mode-locked lasers. The first indications of mode-locking lasers (producing short, powerful pulses of radiation) are found in the work of Gurs and Muller and Statz and Tang in 1964 [25]. The first demonstration of a picosecond pulse train was given by DeMaria, Stetser and Heynau in 1966 [26]. The decades that followed showed the development of the Ti:Sapphire mode-locked laser which significantly reduces the pulse duration; many commercially available systems can produce pulses $<$100 fs [27, 28]. This coupled with the high instantaneous peak power of the pulses produces high efficiencies for nonlinear process (such as TPEF) [28]. Other nonlinear processes that are beneficial for microscopy [1] include second harmonic generation [29, 30],

third harmonic generation [7], and coherent anti-Stokes Raman scattering [9]. Two-photon excitation has many benefits for microscopy, the foremost being the inherent optical sectioning due to fluorescence only being produced in the high intensity region of the focal plane. This leads to less background noise and less photo-bleaching of the sample. Another benefit is the ability to easily separate the excitation signal from the excited signal. For instance, take a TPEF signal initiated by light around 800 nm, the fluorescence would be around half the wavelength, or ∼400 nm, and could easily be filtered out from the 800 nm source for detection. In two-photon microscopy, there is no need for a pinhole to perform the optical sectioning, since the nature of the two-photon fluorescence process intrinsically sections the sample. This work centers on two-photon excitation fluorescence, and applies the technique of SPatIal Frequency modulation for Imaging (SPIFI) to facilitate image acquisition.

1.3 Motivation for Current Work

The essential problem of imaging inside biological samples was separating light carrying information from the sample from light not carrying information. Laser scanning confocal microscopy solved this problem with high illumination optical sectioning of the sample, rejecting out of focus light by use of pinholes. However, the need to scan the sample to obtain a wide-field view introduced a new problem: speed [31]. It takes time to scan [19], and this is a problem confocal and multiphoton microscopists have been working on for the past decade. Numerous scanning methods have been devised [1, 22], some described above. One scanning method of interest is line scanning.

In line scanning, the laser beam is focused by a cylindrical lens to produce a line at focus instead of a point. One of the great benefits of line scanning is that imaging an entire line at once reduces the amount of physical scanning that must be done and thus increases the speed at which images can be taken. Another benefit is since the beam is only focused in one dimension, the power is spread out over the line

and less photodamage is done to the sample [32]. This, however, also leads to a problem: an issue to deal with while applying a line focus to two photon fluorescence is having enough power to generate the fluorescent signal. In 1994, Brakenhoff et. al. used a Ti:Sapphire with a pulse duration of 100 fs, a repetition rate of 250 kHz, and maximum pulse energy of 200 nJ to produce two photon excitation with a line cursor [32]. They reported successful imaging; it was noted, however, that adding a pinhole in the collection direction improved axial resolution, which otherwise would have been decreased due to the line cursor. Carl Zeiss released the line-scanning LSM510 LIVE confocal microscope around 2004 [33]. The system uses anamorphic optics to focus the beam to a line. The excitation is passed through a line-slit (instead of a pinhole) and focused onto a 1 x 512 pixel linear-array CCD. The obvious drawback here is that a slit denies the essential purpose of a pinhole, i.e. that of rejecting light scattered from anywhere but the focal plane [34]. However, this drawback was outweighed by the speed and ease with which a sample could be scanned using a line instead of a point scanner. The idea for a line-scanner was initiated by Maurice in 1968 when he used slit illumination around 100 by 500 micrometers to image endothelial cells in a the cornea [35, 36]. It was developed in practical instruments by Laing and Bourne [37–39]. In 2005, Im et al. produced a line-scanning confocal microscope utilizing an acousto-optical deflector that was capable of 191 frames/s without mechanically moving parts [29]. The measured resolutions were z (depth): 3.3 micrometers, x: 0.7 micrometers, and y: 0.9 micrometers [33]. Their set-up used a cylindrical lens to focus the beam to a line rather that using confocal slits as Maurice, Laing and Bourne used.

There are problems with line scanning, however. The foremost is the need to use a multi-element signal detector, such as a CCD camera. 1969 saw the invention of the charge coupled device, or CCD, by Boyle and Smith [40], which is an array of silicon detectors that allows images to be transmitted to an electronic form for processing

[14]. It is used in myriads of applications, such as spectrometers, telescopes (including extensive use in the Hubble Telescope) and commercial digital cameras, and remains a staple of most confocal microscopes today. Having to image with a multi-element detector has significant drawbacks. The first is noise level. The CCD camera is subject to shot noise, dark noise, and electronic noise which combine to blank out weak signals, such as from dim samples or single molecules [41]. Usually, an image intensifier is combined with a CCD camera to overcome this issue. The problem with most signal enhancers, however, is that the method signal amplification involves loss of spatial precision, and thus the resolution is decreased [41]. The second is an unsolvable problem of loss of resolution due to "cross-talk" between adjacent points in the sample [42]. A photon from one portion of the sample could scatter to a different angle and hit the detector at a different element, and since the spatial information is determined by which element the signal comes from the image is blurred.

The problem of having to use a multi-element detector for line scanning is solved by Futia et al. [31] by using a spinning modulator disk that maps spatial coordinates to modulation frequencies. Each spatial point is modulated to a different frequency, and the emitted fluorescence follows that modulation, allowing the detector to discriminate between spatial points based on the frequency of modulation. The modulation of the fluorescence is used to identify a specific spatial point that the signal intensity at that frequency corresponds to. Thus, the spatial information is encoded in the signal rather than detected by a multi-element detector. Futia et. al. used a 5 mm photodiode as the detector and successfully demonstrated an imaging system with a 177 micrometer spatial resolution. Their work builds on a variety of different methods of imaging [43–45], and stands out as a simple and useful new approach to fluorescent imaging.

The current work provides proof of principle that SPIFI technology can be usefully applied to two-photon fluorescence microscopes. It also summarizes the applications

of SPIFI technology to current real-time three-dimensional imaging systems and details how spatio-temporal focusing can be added to the SPIFI system to increase the axial resolution into diffraction limited domains. These advances will open new pathways to faster image speeds, and simpler implementations of fluorescence microscopy, advancing fields such as solar cell research, medicine, and biological and chemical engineering, in addition to optics and microscopy.

CHAPTER 2

SPIFI THEORY

Futia et. al. introduced a new method of fluorescence imaging with a single-element detector. Multi-element detectors such as a CCD have the drawback of scattering crosstalk between adjacent points in the focal plane, causing the spatial information to blur. This crosstalk can be termed "the scattering ambiguity". Single-element detectors such as photodiodes and Photo-Multiplier Tubes (PMT's) do not have this drawback. Prior to Futia's work, line scanning used multi-element detectors to recover spatial information. However, by frequency modulation of the excitation signal, it is possible to recover spatial information from a time-only signal detected with a photodiode. This allows a line focus geometry to move to essentially photon-counting detection, allowing all the benefits of such a system.

SPatIal Frequency-modulated Imaging, or SPIFI, encodes spatial information into the frequency components of the beam through the use of a spinning modulation disk. The theoretical background for SPIFI imaging is presented, and fluorescent performance characteristics are derived from this background. First the theory of absorption imaging will be discussed, and in the second subsection the theory of fluorescent imaging is reviewed.

2.1 Frequency-Modulated Line Cursor

This section is dedicated to detailing the effect of modulation on the excitation beam.

2.1.1 Theory of Absorption Imaging

Following the development of Futia et. al. [31], the excitation beam can be represented as $E_{excit}(x,t) = E_0 u(x) e^{i\omega_0 t}$ where $u(x)$ is the normalized spatial field

of the beam (a line cursor with a Gaussian shape) and ω_0 is the frequency or color of the excitation light. The object field is the excitation beam with the modulation disk and the object acting on it. Representing the modulation as $m(x,t)$ and the effect of the object, i.e. the object's transmission, as $g(x)$, the object field can be written as $E_{obj}(x,t) = E_0 u(x) m(x,t) g(x) e^{i\omega_0 t}$. What we want is $g(x)$ as this will give us spatial information about the object we are trying to image. Generally, $I(x,t) = \frac{cn\epsilon_0}{2}|E(x,t)|^2$, so

$$I_{obj}(x,t) = I_0 |u(x)m(x,t)g(x)|^2$$

where$I_0 = \frac{cn\epsilon_0}{2}|E_0|^2$, and we can obtain an expression for the signal recorded by the photodiode:

$$s_{obj}(t) = \gamma \int I_{obj}(x,t)dx$$

The scaling constant,γ,includes factors such as detector and system optical efficiency. The modulation used in this work is the same the Futia used in his: $m(x,t) = \frac{w(t)}{2}[1 + \cos(2\pi\kappa x t)]$; $w(t)$ is the finite time-window of the modulator. In other words, it is related to the angular width of the modulator pattern, or $\Delta\theta F_r$.

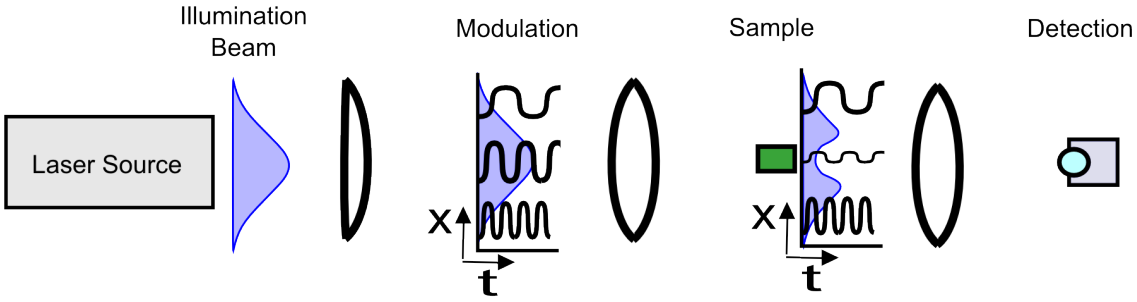

Figure 2.1: SPIFI Theory. The laser source is given by u(x)

With this modulation, the collected intensity is $I_{obj}(x,t) = \frac{1}{4}I_0|g(x)u(x)w(t)|^2[\frac{3}{2} + 2cos(2\pi t\kappa x) + \frac{1}{2}cos(4\pi t\kappa x)]$. The signal $s_{obj}(t)$ can then be broken into three different

components

$$s_{obj}(t) = \frac{1}{2} I_0 \gamma [s_0(t) + s_1(t) + s_2(t)]$$

$s_0(t)$ represents the fundamental of the signal, with $s_1(t)$ and $s_2(t)$ as the first and second harmonics, respectively.

$$s_0(t) = |w(t)|^2 \int \frac{3}{4} |u(x)g(x)|^2 dx$$

$$s_1(t) = \frac{1}{2} |w(t)|^2 \int |u(x)g(x)|^2 e^{2i\pi t\kappa x} dx + c.c.$$

$$s_2(t) = \frac{1}{8} |w(t)|^2 \int |u(x)g(x)|^2 e^{4i\pi t\kappa x} dx + c.c.$$

These differ from Futia's expressions by a factor of $\frac{1}{2}$ which comes from Euler's formula for cosines.

It is helpful to focus on the first harmonic. The center frequency is based on the position of the center of the intensity of the excitation beam on the disk, and is written $x_c = \int x|u(x)|^2 dx$. Shifting to the center by $x' = x - x_c$, the first harmonic signal is

$$s_1(t) = \frac{1}{2} |w(t)|^2 e^{2i\pi t\kappa x_c} \int |u(x')g(x')|^2 e^{2i\pi t\kappa x'} dx' + c.c.$$

Taking the spatial frequency coordinate to be $t\kappa$, the integral in the previous equation takes the form of a spatial Fourier transform. $s_1(t)$ then takes the form

$$s_1(t) = \frac{1}{2} |w(t)|^2 e^{2i\pi t\kappa x_c} \mathcal{F}\left\{ |u(x)g(x)|^2 \right\} + c.c.$$

Writing the Fourier transform as an amplitude and phase of a function $F(\kappa t)$, we see

$$s_1(t) = |w(t)|^2|F(\kappa t)|cos(2\pi f_c t + \angle F(\kappa t))$$

Taking the inverse Fourier transform then recovers our functions $u(x')g(x')$. Doing so results in two sidebands, for negative and positive frequencies, that mirror each other. The positive side band can be written as the convolution between the Fourier transformed modulator window and the functions $u(x')g(x')$.

$$S_{1+}(x') = \mathcal{W}(\kappa x') \circledast |u(x')g(x')|^2 \tag{2.1}$$

Recall that the spatial frequency is κt and thus the transform is between t and $x\kappa$. The transform explicitly is $\mathcal{W}(x') = \int |w(t)|^2 e^{2i\pi t\kappa x'} dt$.

Eq. 2.1 shows that the equivalent "point spread function" is $\mathcal{W}(x') = \mathcal{F}\{|w(t)|^2\}$. Thus, we can recover g(x')u(x') by deconvolving and performing the Fourier transform of the collected time-dependent signal.

2.1.2 Theory of Fluorescence Imaging

The intensity of the collected fluorescence is given by

$$I_{fl}(x,t) = \beta|a(x)|^2 I_{mod}(x,t)$$

with $I_{mod}(x,t) = I_0|u(x)m(x,t)|^2$, β is a scale factor related to the properties of the fluorophore, and $a(x)$ being the absorption (rather that the transmission) of the object's fluorophores. $|a(x)|^2 = \sigma l N(x)$, where $\sigma$is the fluorophore absorption cross section, l is thickness and $N(x)$ is the distribution of fluorophores in the sample. It can be seen that $a(x)$ takes the place of $g(x)$ in the object intensity equation above, and with that substitution the analysis given in 2.1.1 still holds, with the first harmonic signal being

$$s_1(t) = \frac{1}{2}|w(t)|^2 e^{2i\pi t\kappa x_c}\mathcal{F}\left\{|u(x)a(x)|^2\right\} + c.c.$$

2.2 Theory of Modulation Masks

SPIFI is not the first imaging system to use frequency modulated reticles, though it is the first to apply the idea to fluorescence imaging. Sanders et. al. [45, 46] presented in 1991 an imaging system using frequency-modulated reticles, which in 1998 was combined with time-division multiplexing by Bae et. al. [47]. These attempts were mainly used for tracking purposes. Another technique uses spatially-chirped frequencies in a broadband illumination beam [48] to encode spatial information. SPIFI simplifies this approach by instead adding spatially-chirped frequency modulation to the beam, allowing the beam to be in any form and not necessarily broadband [31].

The frequency modulation in SPIFI is achieved through a patterned spinning disk. The pattern used here follows the form

$$m(R,\theta) = \frac{1}{2} + \frac{1}{2}cos[(k_0 + \Delta kR)\theta] \tag{2.2}$$

Inspecting 2.2 we see that the angular frequency is $(k_0 + \Delta kR)$, or in other words, every spatial point R along the line leads to a different modulation frequency. Δk is then the slope of this linear sweep.

Since the beam is essentially one-dimensional, $R \to x$; given f_r as the frequency of reticle rotation, we have $\frac{d\theta}{dt} = 2\pi f_r$ or $\theta = 2\pi f_r t$. Substituting into 2.2 we note that the chirp parameter κ from above is $\kappa = f_r\Delta k$, with an offset $\kappa_0 = f_r k_0$. Here we take $k_0 = 0$. Thus, we arrive at

$$m(x,t) = \frac{1}{2} + \frac{1}{2}cos[2\pi\kappa xt]$$

and we see that adjusting $f_r \Delta k$ controls our center frequency of the modulation band, f_c. Our time window is $T_m = \frac{\Delta\theta}{2\pi f_r}$, where $\Delta\theta$ is the angular width of the linearly-chirped modulator pattern. Our modulation frequency band is given by $\Delta f_m = f_r W \Delta k$ (recall W is the beam width) and our center frequency is $f_c = f_r(\Delta k x_c)$, with x_c as the spatial center of the beam on the modulator disk.

An example of the pattern used is shown in Figure 2.2. The parameters that control the pattern are k_0, Δk and $\Delta\theta$. Δk is the spatial frequency of the modulation at $\theta = 2\pi$. $\Delta\theta$ controls the angular width of the modulation pattern; for $\Delta\theta = 2\pi$, the modulation starts at k_0 and ends in $k_0 + \Delta k$ and for $\Delta\theta = \pi$, the modulation starts at k_0 and ends in $k_0 + \frac{\Delta k}{2}$. The mask used in this work is a Lovell Reticle [49] which has $\frac{\Delta\theta}{2} < \pi$ and mirrors the pattern of the region $0 < \theta < \frac{\Delta\theta}{2}$ to the region $-\frac{\Delta\theta}{2} < \theta < 0$. Thus, while the pattern only goes up to a max spatial frequency of $\Delta k \frac{\Delta\theta}{2\pi}$, the pattern has an angular width of the complete $\Delta\theta$.

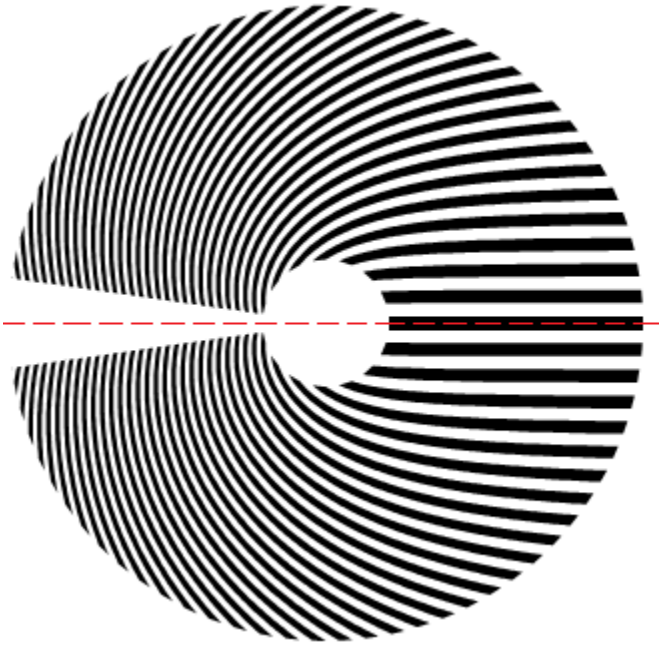

Figure 2.2: Example of frequency-modulation mask. Here the parameters are $\Delta\theta = 6$ rads and $\Delta k = 3mm^{-1}$. The pattern is mirrored across the red dotted line, so that the region $0 < \theta < \frac{\Delta\theta}{2}$ holds the same pattern as the region $-\frac{\Delta\theta}{2} < \theta < 0$.

2.2.1 Fluorescent Imaging Properties

The two most relevant properties of a microscope are spatial resolution and the number of points resolved. In our system, there are three factors that can effect these two properties: the number of points resolved by the mask, the NA of the objective, and how fast we can sample in time due to the data acquisition card (DAQ).

We can approach the problem of obtaining an expression for spatial resolution by viewing the modulation transfer function of the modulator disk, which is the modulus of the optical transfer function, or $MTF = |OTF|$. Analogous to a band-pass filter in an electric circuit, an optical device has a transfer function that defines the spatial frequencies which can pass through the optic. This modulation transfer function is the convolution of the entrance pupil of the optical system with itself. For a square entrance pupil, such as the ones created by the lines on the SPIFI mask, the modulation transfer function (MTF) will look like a triangle. Figure 2.3 shows such an MTF with only the positive frequencies (right half of the triangle) shown. Such an MTF is analogous to the one created by the SPIFI mask.

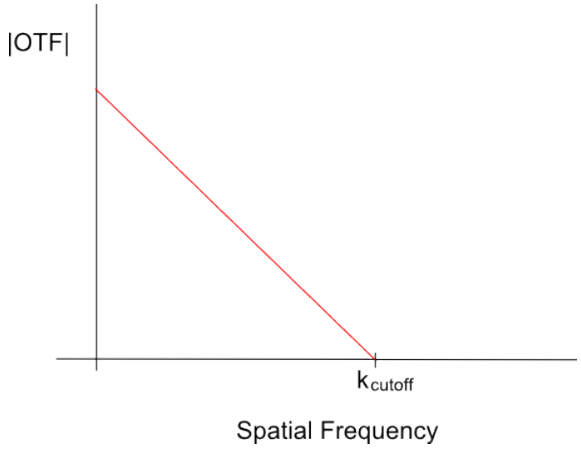

Figure 2.3: Modulation Transfer Function of a SPIFI modulation disk showing only positive frequencies.

By inspection, we can see that there will be a spatial cut-off frequency, k_{cutoff}, which limits the resolution of the system.

The modulator disk acts along the length of the line cursor as a time-varying diffraction grating. That is, it has the effect of placing an image of the grating on the sample. As the disk rotates, the spatial frequency of the mask increases, as shown in Figure 2.4.

The cutoff frequency is the highest spatial frequency that can be sampled, and is k_{max}, as labeled in Figure 2.4 c. The smallest point size that can be measured is then $\frac{1}{k_{max}}$, which gives us our δ_x. k_{max} is dependent on the width of the modulator pattern, $\frac{\Delta\theta}{2\pi}$, and the "chirp" parameter Δk: $k_{max} = \frac{\Delta\theta\Delta k}{2\pi}$.

$$\delta_x = \frac{2\pi}{\Delta\theta\Delta k} \tag{2.3}$$

The number of spatial points sampled is just the highest sampled spatial frequency times the width of the illumination line cursor. $N_{spatial} = k_{max}W$, or

$$N_{spatial} = \frac{W\Delta\theta\Delta k}{2\pi}$$

Note that these two parameters are completely achromatic.

We can relate the frequency cutoff of the MTF to the working f-number of the system by $k_{cutoff} = \frac{1}{\lambda(f/\#)}$. This relates also to the NA of the system: $k_{cutoff} = \frac{2NA}{\lambda}$. Again identifying $k_{cutoff} = \frac{\Delta\theta\Delta k}{2\pi}$,

$$NA = \frac{\lambda\Delta\theta\Delta k}{4\pi} \tag{2.4}$$

The NA, then, depends on the wavelength of our illumination light.

For $\Delta k = 3.7mm^{-1}$ and $\Delta\theta = 6.19$ (the values for the modulator disk used in the current work), NA=0.0014. This is well below the NA of the objective (in this case 0.75) and so the modulator disk becomes the limiting NA of the system. This means that the lateral image resolution is limited by the mask.

The other factor that can impact our resolution is the number of temporally resolved points. This would equal $N_{spatial}$ for an infinitely fast DAQ system. To ensure

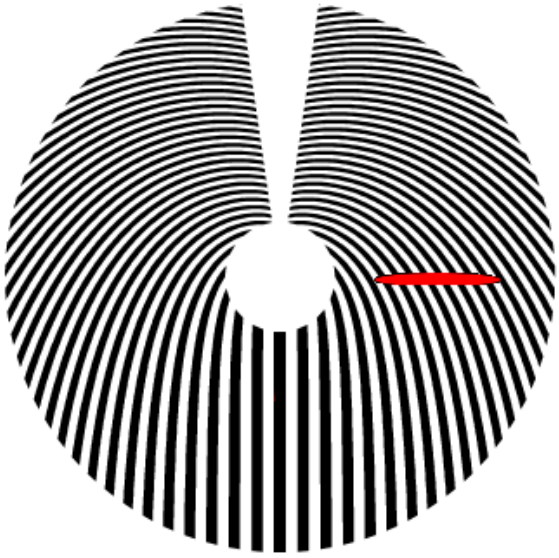

(a) Disk at time $t_i = \frac{\theta_i}{2\pi f_r}$.

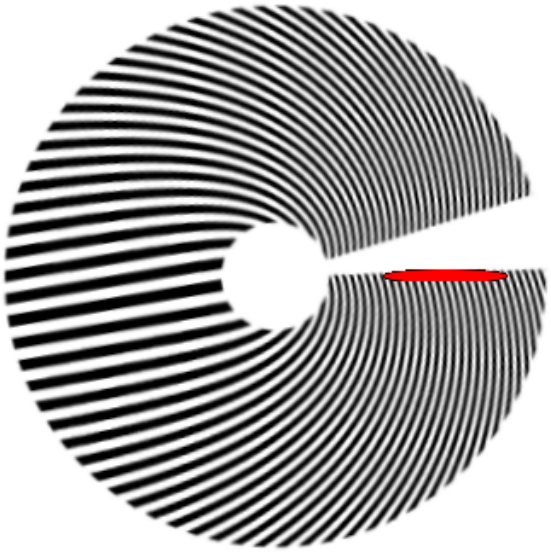

(b) Disk at time $t_{max} = \frac{\theta_{end}}{2\pi f_r}$,where $\theta_{end} = \frac{\Delta\theta}{2}$ which corresponds to the highest spatial frequency modulated by the mask.

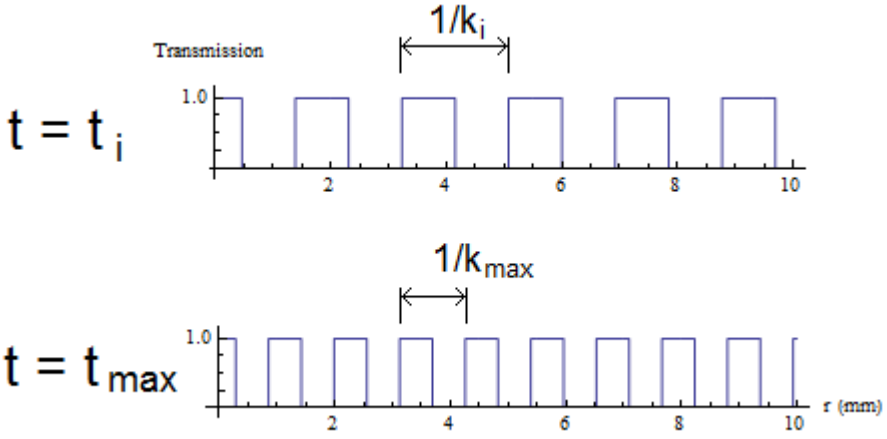

(c)

Figure 2.4: Showing the transmission pattern of the mask along the radial extent of the disk for two different times. This transmission function is for the parameters $\Delta\theta = 6$ rads and $\Delta k = 3mm^{-1}$

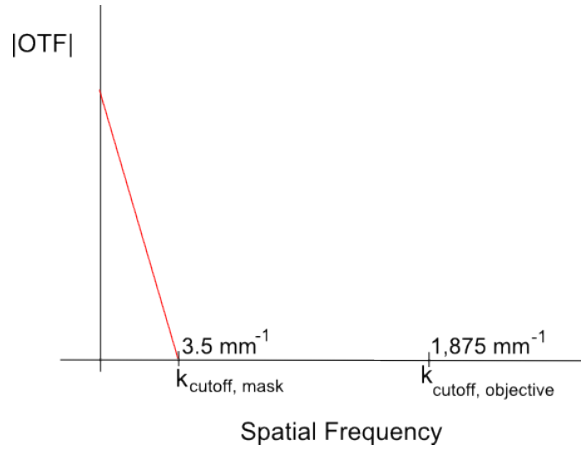

Figure 2.5: Using $k_{cutoff} = \frac{2NA}{\lambda}$ with the NA of the objective, one can compare the cut-off frequencies for the mask and the objective. We use 800 nm light, and the NA of the objective is 0.75. This illustrates that the limiting device is the modulator disk.

that we can treat our DAQ as "infinitely" fast, we compare the highest modulation rate (18 kHz) to the sampling rate of the DAQ (250 kHz or higher). We conclude that in both space and time domains the limiting factor is the modulator.

2.2.2 Beam Spread Due to Modulation Disk

Because of the line cursor geometry used in the set up, the beam focuses differently in each radial direction along the path length of the microscope. This is shown in Figure 2.6.

Figure 2.6 is not completely accurate due to spreading caused by diffraction on the modulation disk. The disk can be thought of as a time varying diffraction grating which causes the beam to diffract at each spatial point along the length of it, as shown in Figure 2.7.

The beam spread can be theoretically calculated from the NA of the modulation mask, given in Eq. 2.4. The NA is a measure of the spread of light from the modulator disk, and so the theory is simply $beam\ spread = distance\ from\ disk \times NA$. In our case, the collimating lens was 10 cm away from the disk, and so the expected beam spread would be 0.14 mm.

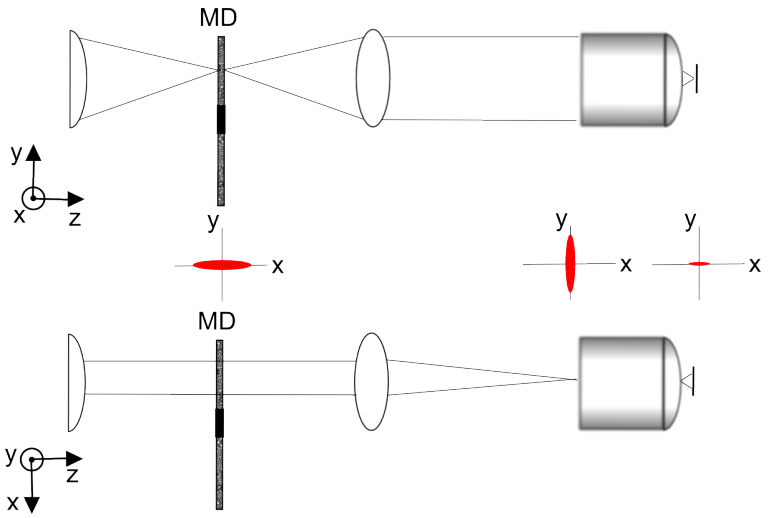

Figure 2.6: The line cursor geometry causes the optics in the system to focus in different places for the two radial directions throughout the path length. The effect of this is to cause the line to extend vertically at the back of the objective. This figure is not completely accurate. (See Figure 2.7)

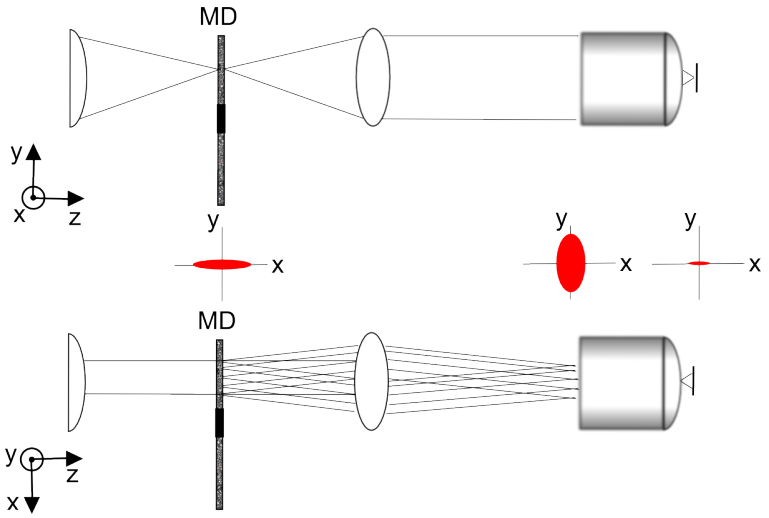

Figure 2.7: The beam will spread due to diffraction at the modulator disk. This causes the line cursor to expand in the non-focusing direction. This spread is expected to fill the back of the objective in the limit of a high density patterned disk, i.e. $\Delta k > 1000 mm^{-1}$.

This spreading is expected to dramatically increase as a function of grating density. For instance, with a Δk of $1000mm^{-1}$, which is possible using lithographic techniques [31] and is the next step in increasing the capability of the SPIFI system, the beam spread would be $\sim$4 cm, plenty to fill the back of the objective in the non-focusing direction. This would also improve the resolution to the single micrometer region. As a note, the limit for filling the back of our Olympus 0.75 NA 20X objective ($\sim$14 mm) is$\Delta k \geq 366mm^{-1}$.

CHAPTER 3

EXPERIMENTAL SET-UP, METHODS, AND RESULTS

Here is presented the SPIFI two-photon microscope in three iterations: a pre-SPIFI two-photon microscope, the same microscope with SPIFI capability added, and a more user-friendly SPIFI TPEF microscope with different scanning ability. Also presented are images taken with each SPIFI-capable iteration.

3.1 Basic Microscope

This section details the first iteration of the SPIFI microscope: one that doesn't have SPIFI capability and is just a two-photon fluorescence microscope.

3.1.1 Set-up

The first iteration is a standard set-up for a two-photon florescence laser-scanning microscope [2], shown in Figure 3.1. It includes a beam expander (L1 and L2), the cylindrical lens (C1) to produce the line cursor, a one-to-one telescope to image the beam to the back of the objective (L3 and L4), and the appropriate lens (L5) to collimate the beam before entering the back of the objective (a 0.75 NA Olympus 20X). In this first iteration the fluorescence was measured in the transmission direction with a Hamamatsu R7400P PMT, requiring the use of the collection objective. The illumination source is a Ti:Sapphire oscillator with a 19 MHz repetition rate, 50 fs pulse duration, and average power $\sim$180 mW.

3.1.2 Beam Size Adjustment to Overfill Objective

In order to achieve diffraction limited performance from the objective, the illuminating source beam needs to fill the back of the objective. The Ti:Sapphire beam was expanded through the use of a telescope placed in the entering path of the beam, before the cylindrical lens.

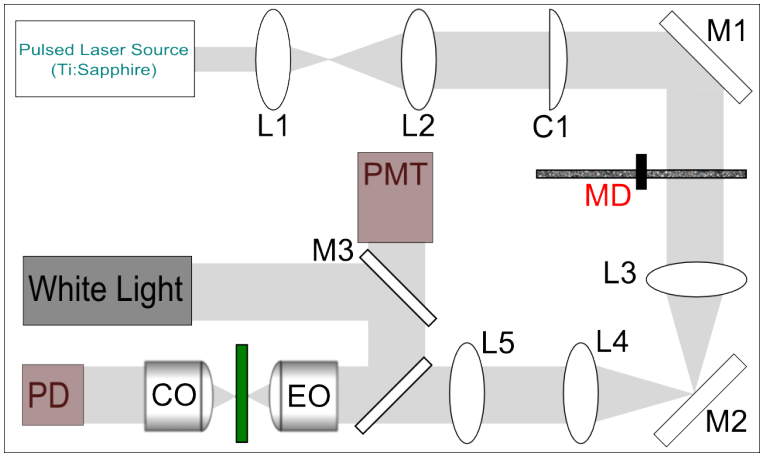

Figure 3.1: Initial Set-up. L1: 51 mm singlet. L2: 400 mm singlet. C1: 100 mm cylindrical lens. L3: 100 mm singlet. L4: 100 mm singlet. L5: 160 mm singlet. Before the objective is a dichroic (R: 400-600 nm, T: 700-1000 nm). EO: Olympus 20X 0.75 NA UPlanSApo. CO: 30X 0.62 from Newfocus. PMT was a Hamamatsu R7400P PMT capable of being biased up to 1000V. PD: Silicon photodiode. The first, non-SPIFI set up did not have the modulation disk (MD) in it. The modulation disk was added later.

The beam size of the original microscope [Figure 3.1] was measured by placing a pinhole just before the objective and picking off the collimated light, sending it through a 50 cm lens into a Powermax 500A laser power meter. The pinhole is then dialed down until the powermeter reads half of the original power. The pinhole diameter (measured with a micrometer) is the spot-size of the beam. The cylindrical lens was removed from the set-up to produce the best measurement of beam expansion at the back of the objective. In order to preserve collimation at the back of the objective, the first lens in the one-to-one telescope also needed to be removed. The two measurements of beam size that follow were done with these two lenses removed from the microscope.

Using this method, the original beam size was found to be approximately 5 mm, FWHM. The back of the Olympus 20X objective was measured to be approximately 14 mm.

Choosing appropriate lenses for the telescope was a matter of three things: what was on hand, what would fit into the microscope space, and how powerful the lenses

could be before introducing significant aberrations in the beam shape. Taking these three considerations into hand, a 51 mm and a 400 mm lens were selected, with a magnification of 7.8x when placed 451 mm apart from each other. By eye, this filled the back of the objective. The measured beam size (using the same method as above) was approximately 12 mm, FWHM.

It should be noted here that with the cylindrical lens produces a line cursor, which will only fill the objective in one radial direction, severely under-filling it in the perpendicular axis. The spinning modulator disk will create a spread in this under-filled axis which is proportional to the density of the mask lines (see Section 2.2.2). Though the work in this thesis uses a modulator mask that does not fill the objective in that axis, future work will use a higher density mask that will spread the beam enough at the back of the objective that it will fill the objective in both directions.

3.1.3 Scan Optic: Mirror

The mirror M2 was replaced with a voltage-controlled galvanometric scan mirror driven by a function generator capable of producing both AC and DC signals and timing signals for image taking. With the line cursor set-up, only a one dimensional scan is needed.

3.2 SPIFI Microscope

This section is the second iteration of the SPIFI Microscope, where the basic microscope detailed in Section 3.1 is improved with SPIFI.

3.2.1 Set-up

To introduce SPatIal Frequency-modulated Imaging to a line cursor two-photon microscope, a modulator mask is added of the type described in Section 2.2. The type used for the present work is described by Eq. 2.2 with parameters $\Delta\theta = 6$ radians, $\Delta k = 7mm^{-1}$, and $k_0 = 0$; it is the same pattern used by Futia in 2011. The

modulator mask is placed at the focus of the cylindrical lens and 10 cm away from the first lens of the one-to-one telescope. The modulator mask is spun by a motor controller connected to the imaging software through a NI DAQ 4643. The imaging software and set-up for imaging is described in Section 3.3.

In this set-up, the two-photon signal is imaged with the PMT in the epi-direction through the use of a dichroic mirror placed just before the objective. The fundamental is imaged in transmission with a photodiode. A white light camera was also inserted into the set-up to aid in the imaging and microscope characterization process.

3.2.2 Field of View Calculation

To determine field of view, a sample of gold mesh mounted on a CHROMA slide was imaged in both the fundamental and the two-photon signal. The image is then analyzed to determine the number of meshes that appear in the image.

First, a determination of the mesh grid size is made. The particular grid used was oriented on the sample slide at a diagonal, so the measurement was from corner to corner of one square "hole". Using the white light camera, an image of the mesh was displayed on-screen. A mark was made with scotch tape and a vis-a-vis pen on one corner of the square mesh hole. Then, the sample was scanned manually measuring the distance for the opposite corner to reach the mark on the scotch tape. This was done for a hole and the same process was repeated for the space between holes (the width of the actual mesh line). This is depicted in Figure 3.2. The hole size was 0.025 mm and the mesh line size was 0.010 mm.

Using these measurements to calibrate the images shown in Figure 3.3 (a) and (b), it is shown that the horizontal field of view for the SPIFI microscope with the current beam size and modulation mask is $225\mu m$ for the fundamental and $150\mu m$ for the TPEF signal.

From the figure it is observed that the intensity drops off significantly for the TPEF signal compared to the fundamental. This is because the interaction resulting in the

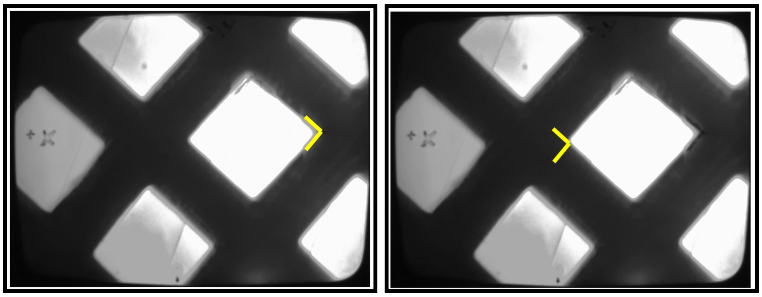

Figure 3.2: Depiction of How Grid Size was measured. Each hole is 0.025 mm (from side to side, not corner to corner) and the mesh line is 0.010 mm wide.

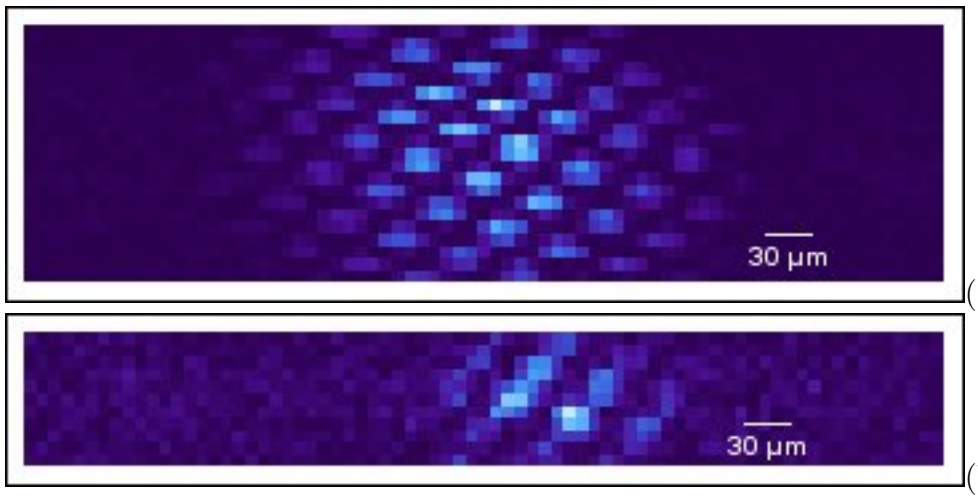

(a)

(b)

Figure 3.3: (a) is an image obtained with the fundamental beam. (b) is an image obtained with TPEF.

two-photon signal requires two incident photons instead of one, so the region being excited by the illumination beam is limited to the focal region where the intensity of the laser beam is such that the probability of two-photon interaction is high.

3.2.3 Lateral Resolution Measurement

A 1951 US Air Force Resolution Test Target was used to determine the lateral resolution of the SPIFI microscope. Using the fundamental beam, the target was scanned through the resolution groups from largest to smallest until the space between the lines could no longer be distinguished on the SPIFI set-up in the SQUID interface (see Section 3.3). This smallest group was found to be between group Five-1 and group Five-2; group Five-2 corresponds to 10 μm (measured by the same method as the gold mesh squares). Figure 3.4 shows an example of a typical SPIFI SQUID line output as well as the output for group Five-2 of the USAF target. It should be noted that group Five-1 was scratched on the target and thus couldn't be imaged. The group Five-2 target lines could just barely be resolved, and so the actual value for the resolution is between these two values.

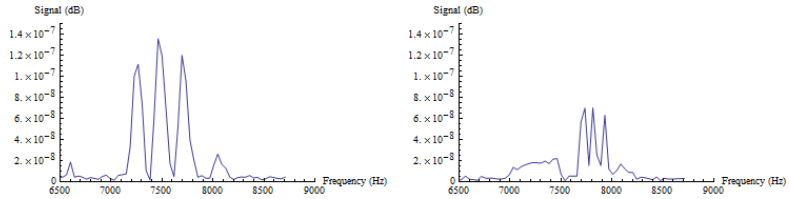

(a) (b)

Figure 3.4: (a) Typical SPIFI Line Out. This is of Group 4-1 of the USAF Resolution target. (b) Line out data for the smallest just discernible group on the USAF Resolution target: Group 5-2, corresponding to a resolution of 10 μm .

By 2.3, we should obtain a resolution of ∼13.7 μm, taking the magnification of the microscope to be 20X (from the Olympus objective). The measured value is close to what we expect, then, from our modulation disk.

3.2.4 Two-photon Sectioning Measurements

Figure 3.1shows the experimental set-up of the sectioning measurements. Note that the modulation disk is not in place yet. The line cursor itself is what needs to be characterized. Sectioning measurements are done by sweeping a fluorescent sample through the focus and measuring the output. The illumination source was a mode-locked Ti:Sapphire diode pumped laser running at 184 mW output, 19 MHz shot rate, 50 fs pulses. At the sample the laser power was 143 mW. The fluorescence signal was detected by a PMT with a 600 V bias and reading to a voltmeter. The linearity of the signal was confirmed by measuring the unfiltered power just before the objective lens and the collection voltage read by the PMT; a half-power N.D. filter was then placed in the beam path and the power and collection voltage were read again. It is expected that the ratio of filtered power to unfiltered power would be half; and the intensity of two-photon fluorescence is proportional to the excitation intensity squared, the ratio of filtered to unfiltered collection voltage would be approximately 1/4. Experimental measurements confirmed this was the case.

A Chroma slide was scanned axially (z-direction) in submicron steps by means of a Thorlabs Stepper Motor Controller (BMS001). At each step, the collection voltage of the PMT was recorded with a multimeter. Taking the derivative of this curve, a representation of the axial focus can be obtained. From this curve, the axial resolution of the SPIFI Two-Photon Microscope was $30\mu m$.

3.3 Imaging

The output of either the photodiode or the PMT was sent through the NI DAQ (a National Instruments USB DAQ 4643) into the SQUID program (see Section 3.3.1 and Appendix B). In the case of the PMT, a variable load was attached in parallel for reasons explained later in this section. Figure 3.5 shows a pin-out of the NI DAQ connections, including the motor controller.

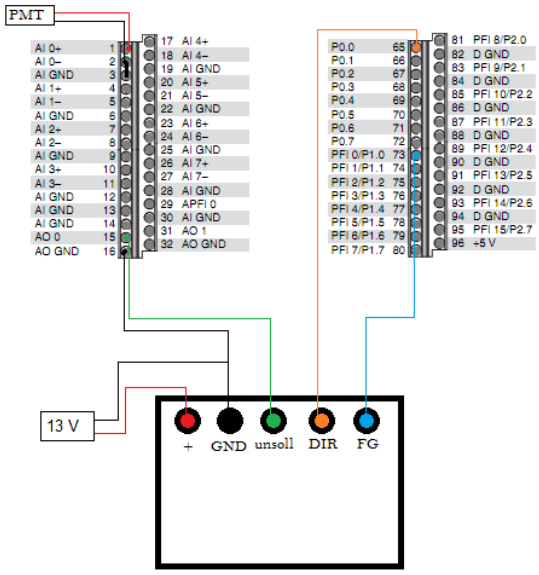

Figure 3.5: Pin-out for the NI-DAQ and the Faulhaber Motor Controller

3.3.1 SQUID Program and Image Construction Using Mathematica

The imaging software used was SQUID, a program developed by David Winters and used by Futia et. al. in their 2011 work [31]. SQUID decodes the spatial information in the time-varying signal by taking the Fourier transform of the input signal and deconvolving from the modulation window. Taking one line of image at a time, the data is saved as .csv file. This file is then imported into Mathematica and the data is directly plotted line by line to form the image. The code is shown in Appendix A.1. The Fourier transform of the time-varying signal gives the intensity of each spatial point along the cursor; thus, the images obtained are intensity maps of the strength of the two-photon florescence or scattered fundamental beam.

Additional information about the SQUID program can be found in Appendix B.

3.3.2 Estimating the Detected TPEF Signal

The most important contributing factor was the variable load placed in parallel with the DAQ on the output of the PMT. The load which maximized signal strength was 22 $k\Omega$. The reason this increased signal strength can be seen from a considera-

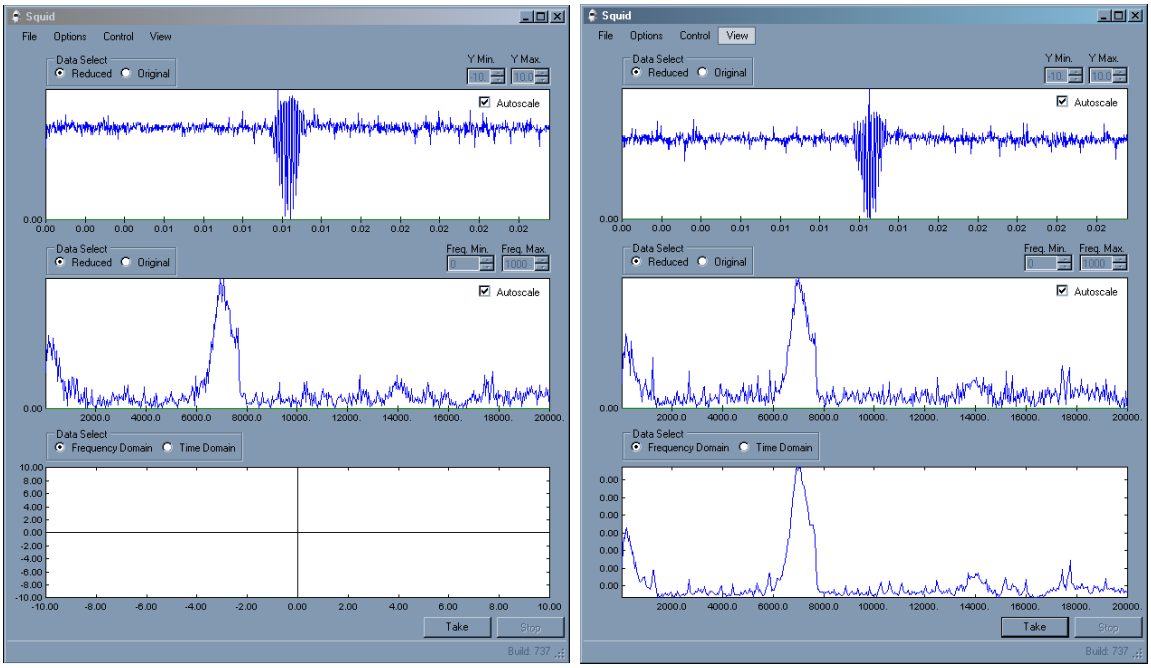

(a) (b)

Figure 3.6: Screenshots of the SQUID program. (a) The top pane shows the frequency-modulated signal from the photo diode. The middle pane shows the Fourier transform of that signal, in this case an image of just the illumination beam from an 800 nm diode laser running at 300 mA. The bottom pane is blank here because the "Take" button has not yet been pressed. Once the button is pressed, both the raw signal and the Fourier transform data is saved to a buffer, and can be selected to be viewed in the bottom frame. Once data is in the buffer it can be saved. (b) It is possible to accumulate traces with the SQUID program. One such accumulated trace of the same laser beam as in (a) is shown in the bottom pane as data that was "Taken".

tion of the current coming off of the PMT. To elucidate this, consider an estimation of the detected TPEF signal. This calculation involves the efficiency of the sample in converting the illumination photons into imaging photons. This sample efficiency depends on the photons per pulse of the laser and factors such as the the cross section of absorption, quantum efficiency, and concentration of fluorophores that involve the fluorescent dye used in the sample. Since this work used Chroma slides as the fluorescent material, these factors are unknown. Therefore we use a modest estimate of a sample efficiency of 0.01 emitted photons per excitation pulses. The laser in use has a 20×10^6 repetition rate. Then we need to consider factors involving the efficiency of the collection optics used in the microscope. This includes the objective (efficiency 0.90), the dichroic used in reflecting the signal photons to the detector (0.90 at 400 nm), and the lens used to focus the photons onto the detector (an achromat with efficiency $\sim$0.98). The PMT used was a Hamamatsu R7400P and has a quantum efficiency of about 0.10. These efficiencies combine to produce a total optical efficiency of $0.9 \times 0.9 \times 0.98 \times 0.1 = 0.08$. Then take the sample efficiency, shot rate, and optical efficiency to determine the number of signal photons per sec: $0.08 \times 0.01 \frac{photons}{pulse} \times 20 \times 10^6 \frac{pulse}{sec} = 1.6 \times 10^6 \frac{photons}{sec}$. The gain on the PMT is 10^6 when biased at 800 V. (In this work the PMT was rarely biased above 800 V). This yields a current of $1.6 \times 10^6 \frac{electrons}{sec} \times 10^6 \times 1.6 \times 10^{-19} \frac{coulombs}{electron} = 2.56 \times 10^{-7} A$. Placed across a load of 50 Ω, that is 0.0128 mV. Placed across a 22 $k\Omega$ load (such as the one used in the SPIFI set-up), we have 5.6 mV, a drastic increase.

3.4 A Simpler Design

The SPIFI set up has just recently gone through another iteration to make it simpler in set up and user-friendly. The final set-up (Figure 3.7) uses computer controlled stage scanning and does away with the scan mirror and removes the need for the one-to-one telescope. The beam is expanded (using the same two lenses) before entering the microscope, so the only optics in the current SPIFI microscope are the

cylindrical lens, the modulation disk, the collimating lens before the objective, and the two objectives. In this set-up a PMT is used in transmission.

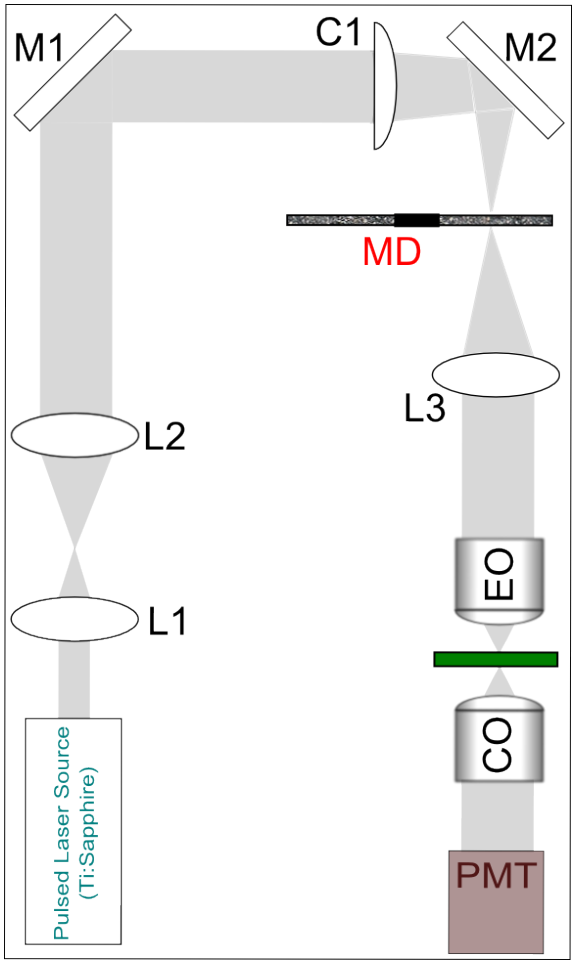

Figure 3.7: A Simpler Design.

With this set-up, a two-photon excitation fluorescence image of onion skin cells were obtained (Figure 3.8), proving once again that the SPIFI method can be used to effectively image with two-photon techniques.

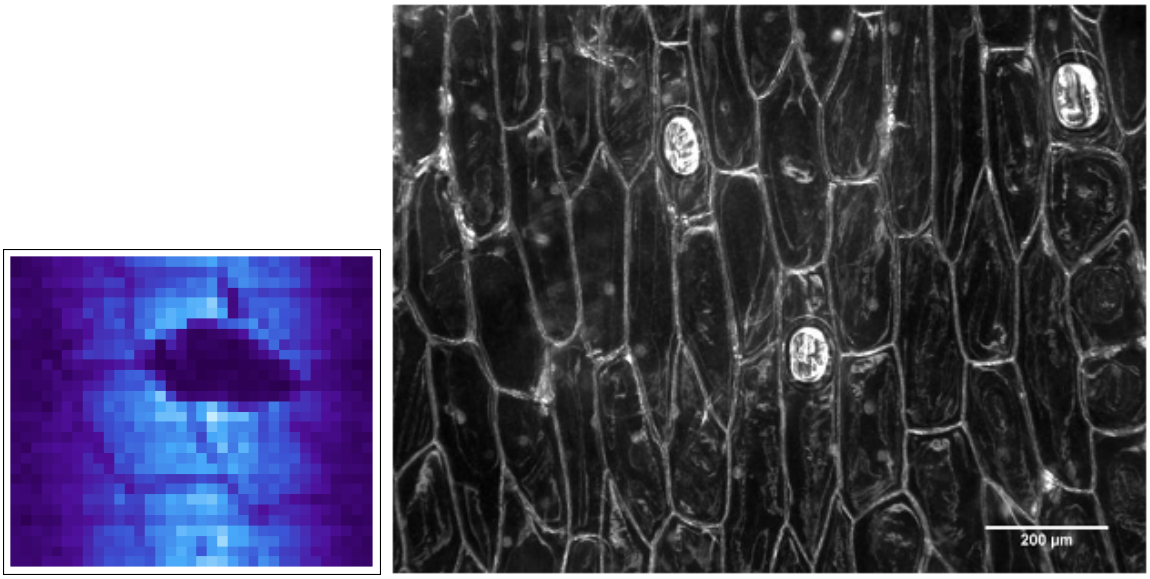

(a) (b)

Figure 3.8: (a) Two-photon fluorescence SPIFI image of Onion skin cells (raw data). (b) Dark field image of same thing.

CHAPTER 4

CONCLUSION AND FUTURE POSSIBILITIES

Here we review what has been accomplished and detail future work that can be done on the SPIFI Microscope.

4.1 Review of Accomplished Work

A functional two-photon microscope utilizing a line-cursor geometry with single-element detection has been constructed and characterized. This is possible using a frequency modulated reticle placed in the image plane of a cylindrical lens. A review of the measured characteristics of the several iterations of the SPIFI TPEF microscope are given in Table 4.1.

Table 4.1: Review of SPIFI TPEF Microscope Characteristics

Characteristic	SPIFI Fundamental	SPIFI TPEF
Field of View	$225\mu m$	$150\mu m$
Lateral Resolution	$10\mu m$	$10\mu m$
Magnification	20X	20X

In addition, sectioning measurements were performed which revealed a z-resolution of 30 μm.

4.2 Applications in Real-Time 3D Imaging

The first real-time multiphoton microscope was in fact a line cursor geometry set-up [32]. It used a line-slit pinhole to counter cross-scattering in one axis, and required a multidimensional CCD detector. This geometry was preferred initially because it allowed single-axis scanning which decreased imaging time drastically. However, this geometry compromised axial resolution because of low NA in the axis that was under-filled.

To preserve axial resolution while still attaining high frame rates, multi-focal multiphoton microscopes were developed. In these systems, multiple focal spots are created through a myriad of mechanisms, microlens arrays being the foremost. The task was to pack as many focal point spots into a sample area as the laser power could sustain. The first attempts actually exhibited lower axial resolution due to interference between the spots, which was remedied by delaying the individual spots by several times their pulse duration, achieving resolution equal with that of a single diffraction-limited laser focus [50, 51].

These multi-focal systems then had the challenge of only being useful for very thin scattering specimens because they require two-dimensional detectors. The approach to deal with this scattering issue has been to switch from integrated detection to photon-counting [52]. This completely erases the scattering ambiguity and allows multiple focal planes to be imaged in a single transverse scan. Innovations also include dynamic repositioning of individual focal planes via remote focusing [53].

These volumetric scanning multi-focal systems could be easily modified to incorporate a SPIFI set-up, which would simplify the geometry and increase scan rates. In addition, there is a notable consequence of using a line scanning cursor. As shown in Figure 2.7, the line cursor incident on the diffraction grating acts as a multiple beam sources. With high density masks, this could effectively enable the use of hundreds or thousands of beams instead of the six beams that Sheetz et. al. used in their work on multi-focal systems[54].

4.3 Adding Spatio-Temporal Focusing to Increase Sectioning Capability

A recent innovation in sectioning capability could also be applied to the SPIFI microscope to improve axial resolution. That innovation is spatio-temporal focusing. Oron et. al. [19] and Zhu et. al. [55] produced simultaneous demonstrations of spatio-temporal focusing in 2005 by placing a diffraction grating so that it will be imaged onto the back of the objective. This focuses the beam temporally and has

been shown to improve depth resolution to 1.5 micrometers in line-scanning systems [56].

The use of spatio-temporal focusing (STF) in microscopy was initiated by Oron, Tal and Silberberg [19] and independently by Zhu et. al. [55]. Zhu's interest in STF was to reduce the background excitation produced out-of-focus deep inside samples.

Oron, Tal, and Silberberg, independently of and at the same time as Zhu et. al., investigated the uses of temporal focusing for removing the need to scan samples. They reported a significant increase in axial resolution in both TPEF and THG.

Spatio-temporal focusing works by separating the frequencies of a laser pulse spatially with a grating, collimating them, and recombining them with an objective or other lens. The different frequencies overlap only in the focal plane (by Fermat's principle), so the pulse width is shortest only in that plane. Since the axial focus is tighter, the amount of sectioning capability is increased.

This spatio-temporal focusing effect can be employed easily in the current SPIFI set-up simply by placing a transmission diffraction grating at an image plane of the frequency-modulated line cursor. This would allow diffraction limited axial resolution. Since this set-up is a stage-scanner, this is all that would be needed. With a beam-scanning microscope, caution would need to be taken with how the diffraction grating is oriented due to Braggs angle.

4.4 High Density Mask

As explained in Section 2.2, a higher density mask would improve lateral resolution to $\sim 1\mu m$ and would fill the back of the objective. At this point the limiting NA would need to be reanalyzed with the diffractive effects of the mask in mind, i.e. utilizing the standard equation $sin(\theta_i) + sin(\theta_m) = \frac{m\lambda}{d}$.

It is clear, however, that the next steps in using SPIFI are to improve axial resolution using spatio-temporal focusing and to employ higher density disks to study the effects of such.

REFERENCES CITED

[1] Carriles et. al. Invited review article: Imaging techniques for harmonic and multiphoton absorption fluorescence microscopy. *Rev. Sci. Instrum.*, **80**(8), 2009.

[2] K. E. Sheetz and J. Squier. Ultrafast optics: Imaging and manipulating biological systems. *J. Appl. Phys.*, **105**:051101, 2009.

[3] M. Kirber R. Reich B. Kosicki W. McGonagle K. Bahlmann, P. T. C. So and K. Bellve. Multifocal multiphoton microscopy (mmm) at a frame rate beyond 600 hz. *Opt. Express*, (15).

[4] K. E. Sheetz et. al. Advancing multifocal nonlinear microscopy: development and application of a novel multibeam yb:kgd(wo4)2 oscillator. *Opt. Express*, **16** (22):17574, 2008.

[5] M. Straub and S. W. Hell. Multifocal multiphoton microscopy: A fast and efficient tool for 3-d fluorescence imaging. *Bioimaging*, (6):177.185, 1998.

[6] N. Olivier et. al. Cell lineage reconstruction of early zebrafish embryos using label-free nonlinear microscopy. *Science*, **329**(5994):967–971, 2010.

[7] A. Royon et. al. Third-harmonic generation microscopy for material characterization. *J. Opt. Soc. Korea*, **10**:188–195, 2006.

[8] A. Gruber M. Barth, R. Schuster and F. Chicos. Imaging single quantum dots in three-dimensional photonic crystals. *Phys. Rev. Lett.*, **96**(24), 2006.

[9] D. Schafer et. al. Coherent anti-stokes raman scattering microscopy for quantitative characterization of mixing and flow in microfluidics. *Opt. Lett.*, **34**(2): 211–213, 2009.

[10] D. N. Vitek et. al. Temporally focused femtosecond laser pulses for low numerical aperture micromachining through optically transparent materials. *Opt. Express*, **18**(17):18086–18094, 2010.

[11] E. Mazur D. N. Fittinghoff, C. B. Schaffer and J. Squier. Time-decorrelated multifocal micromachining and trapping. *IEEE J. Sel. Top. Quantum Electron*, (7):559–566, 2001.

[12] S.G. Lipson A. Lipson and H. Lipson. *Optical Physics, 4th ed.* Cambridge University Press, 2011.

[13] D. Whitehouse. World's oldest telescope?, July 1, 1999.

[14] J. N. Mait. A History of Imaging: Revisiting the Past to Chart the Future. *Optics and Photonics News*, **17**(2):22–27, 2006.

[15] J. Gribbin. *The Scientists*. Random House, New York, 2002.

[16] Hooke. *Micrographia*. 1665.

[17] M. Minsky. Microscopy apparatus. *US patent 3,013,467*, Dec. 19 1961.

[18] R. H. Webb. Confocal optical microscopy. *Rep. Prog. Phys.*, **59**:427–471, 1996.

[19] E. Tal D. Oron and Y. Silberberg. Scanningless depth-resolved microscopy. *Opt. Express*, **13**(5):1468–1476, 2005.

[20] P. Nipkow. Elektrisches teleskop, 1884.

[21] P. Davidovits. Scanning laser microscope for biological investigations. *Appl. Opt.*, **10**:1615–1619, 1971.

[22] P. Davidovits and M.D. Egger. *Nature*, (223):831, 1969.

[23] Denck et. al. Two-photon fluorescence scanning microscopy. *Science*, **248**:73–75, 1990.

[24] K. E. Reickhoff W. L. Peticolas, J. P. Goldsborough. Double photon excitation in organic crystals. *Phys. Rev. Lett.*, **10**:43, 1963.

[25] H. A. Haus. Mode-Locking of Lasers. *IEEE Journal of Selected Topics in Quantum Electronics*, **6**(6):1173–1185, 2000.

[26] D. A. Stetser A. J. D. DeMaria and H. Heynau. Self mode-locking of lasers with saturable absorbers. *Phys. Lett.*, **8**(174), 1966.

[27] T.B. Norris J. K. Rhee, T. S. Sosnowski. Chirped-pulse amplification of 85-fs pulses at 250 khz with third order dispersion compensation by use of holographic transmission gratings. *Opt. Lett.*, **19**:1550–1552, 1994.

[28] J.G. White P. F. Curley, A. I. Ferguson and W.B. Amos. Application of a femtosecond self-sustaining mode-locked ti:sapphire laser to the field of laser scanning confocal microscopy. *Opt. and Quant. Elec.*, **24**:851–859, 1992.

[29] D. Oron and Y. Silberberg. Harmonic generation with temporally focused ultrashort pulses. *J. Opt. Soc. Am. B*, **22**(12):2660–2663, 2005.

[30] Rebecca M. Williams Warren R. Zipfel and Watt W. Webb. Nonlinear magic: multiphoton microscopy in the biosciences. *Nature Biotechnology*, **21**:1369–1377, 2003.

[31] D. G. Winters G. Futia, P. Schlup and R. A. Bartels. Spatially-chirped modulation imaging of absorbtion and fluorescent objects on single-element optical detector. *Opt. Express*, **19**(2):1626–1640, 2011.

[32] T. Norris A. C. Bliton M. H. Wade G. J. Brakenhoff, J. Squier and B. Athey. Real-time two-photon confocal microscopy using a femtosecond, amplified ti:sapphire system. *J. Microsc.*, **181**:253–259, 1996.

[33] K-B. Im et. al. Simple high speed confocal line scanning microscope. *Opt.Express*, **13**(13):5151–5156, 2005.

[34] A. Mendez-Vilas and J.Diaz (Editors). *Modern Research and Educational Topics in Microscopy, 2007 Ed.* Formatex, 2007.

[35] C. J. Koester. Scanning mirror microscope with optical sectioning characteristics: applications in ophthalmology. *App. Opt*, **19**(11):1749–1757, 1980.

[36] D. Maurice. *Experientia*, **24**:1094, 1968.

[37] H. M. Leibowitz R. A. Laing, M. M. Sandstrom. *Arch. Ophthalmol*, **93**:143, 1975.

[38] W. M. Bourne and H. E. Kaufman. *Am. J. Ophthalmol*, **81**:319, 1976.

[39] B. E. McCarey W. M. Bourne and H. E. Kaufman. *Trans. Am. Acad. Ophthalmol. Otolaryngol*, **81**:OP–743, 1976.

[40] G. E. Smith. The Invention and Early History of the CCD. *Nuclear Instruments and Methods in Physics Research A*, **607**(1):1–6, 2009.

[41] J. B. Pawley (Editor). *Handbook of Biological Confocal Microscopy, 3rd ed.* Springer, New York, 2006.

[42] E. Chandler et. al. High-resolution mosaic imaging with multifocal, multiphoton photon counting microscopy. *Appl. Optics*, **48**(11):2067–2077, 2009.

[43] M. A. A. Neil R. Juskaitis, T. Wilson and M. Kozubek. Efficient real-time confocal microscopy with white light sources. *Nature*, **383**:804–806, 1996.

[44] R. Heintzmann and P. A. Benedetti. High-resolution image reconstruction in fluorescence microscopy with patterned excitation. *Appl. Opt.*, **45**:5037–5045, 2006.

[45] C. E. Halford J. S. Sanders, R. G. Driggers and S. T. Griffin. Imaging with frequency-modulated reticles. *Opt. Eng.*, **30**:1720–1724, 1991.

[46] Glenn D. Boreman Douglas Lattman Kevin F. Williams Ronald G. Driggers, Carl E. Halford. Parameters of spinning fm reticles. *Applied Optics*, **30**(7): 887–895, 1991.

[47] Duck-Soo Noh Soo-Joong Kim Jang-Keun Bae, Yang-Hoi Doh. Imaging system using frequency modulation/time division multiplexing hybrid reticle. *Optical Engineering*, **37**(7):2119–2123, 1998.

[48] Benjamin J. Vakoc Brett E. Bouma Jason T. Motz, Dvir Yellin and Guillermo J. Tearney. Spectral- and frequency-encoded fluorescence imaging. *Optics Letters*, **30**(20):2760–2762, 2005.

[49] D. J. Lovell. Electro-optical position indicator system. *U.S. Patent*, **2,997,699**, 22 Aug 1961.

[50] J. Squier A. H. Buist, M. Muller and G. J. Brakenhoff. Real time two-photon absorption microscopy using multi point excitation. *J. Microsc. (Oxford)*, **192** (2):217–226, 1998.

[51] S.W. Hell V. Andresen, A. Egner. Time multiplexing and parallelization in multifocal multiphoton microscopy. *J. Opt. Soc. Am. A*, **17**(7):1192–1201, 2000.

[52] Erich E. Hoover Jeff A. Squier Ramon Carriles, Kraig E. Sheetz and Virginijus Barzda. Simultaneous multifocal multiphoton, photon counting microscopy. *Optics Express*, **16**(14):10364–10371, 2008.

[53] Eric V. Chandler Anding Luo Jeffrey J. Field Kraig E. Sheetz Anne W. Sylvester Erich E. Hoover, Michael D. Young and Jeff A. Squier. Remote focusing for programmable multi-layer differential multiphoton microscopy. *Biomedical Optics Express*, **2**(1):113–122, 2011.

[54] Ramon Carriles David Kleinfeld Kraig E. Sheetz, Erich E. Hoover and Jeff A. Squier. Advancing multifocal nonlinear microscopy: development and application of a novel multibeam yb:kgd(wo4)2 oscillator. *Optics Express*, **16**(22): 17574–17584, 2008.

[55] G. Zhu et. al. Simultaneous spatial and temporal focusing of femtosecond pulses. *Opt. Express*, **13**(6):2153–2159, 2005.

[56] D. Oron E. Tal and Y. Silberberg. Improved depth resolution in video-rate line-scanning multiphoton microscopy using temporal focusing. *Opt. Lett.*, **30**(13).

APPENDIX A - MATHEMATICA CODE

Mathematica code for importing and forming and image from data saved from the SQUID program is included here. Also, the code used to process the sectioning data is also presented.

A.1 Importing and Forming and Image

The following function imports one file (one line of the image) and crops out all the unused frequencies (as set by the parameters "cutLeft" and "cutRight"). It then returns a Mathematica list of the imaging data nicely cropped.

```
getData[fileName0_] := Module[{fileName = fileName0, data, dataArray},
data = Import[fileName];
data = Table[data[[i, {3, 4}]], {i, 1, Length[data]}];
data = Drop[data, cutLeft];
data = Drop[data, -cutRight];
dataArray = Table[data[[i, 2]], {i, 1, Length[data]}]
];
```

This next bit of code takes all the separate line-out files and puts them into one 2-D matrix so that each matrix element has an intensity associated with it. While in this example I use only ten files, 30 files is typical.

```
numOfFiles = 10;
dataArray2 = Table[{}, {i, 1, numOfFiles}];
filePath = "C:\\Users\\YourName\\Data_From_SQUID\\etc\\";
```

```
dataArray2[[1]] = getData[filePath <> “01.csv”];
dataArray2[[2]] = getData[filePath <> “02.csv”];
dataArray2[[3]] = getData[filePath <> “03.csv”];
dataArray2[[4]] = getData[filePath <> “04.csv”];
dataArray2[[5]] = getData[filePath <> “05.csv”];
dataArray2[[6]] = getData[filePath <> “06.csv”];
dataArray2[[7]] = getData[filePath <> “07.csv”];
dataArray2[[8]] = getData[filePath <> “08.csv”];
dataArray2[[9]] = getData[filePath <> “09.csv”];
dataArray2[[10]] = getData[filePath <> “10.csv”];
```

Then, the 2-D array is plotted with the graphical “spatial position” given by the matrix indicee, and the value at that indicee as the intensity.

```
ArrayPlot[dataArray2, ColorFunction -> “DeepSeaColors”]
Export[filePath <> “image_name.format”, %]
```

A.2 Sectioning Measurement Code

Code snippet showing how the numerical derivative of the data was taken:

```
SymDer[data0_] := Module[{data = data0},
derOfData = Table[{data[[i, 1]], 0}, {i, 1, Length[data]}];
For[i = 1, i < Length[data], i++,
If[data[[i + 1, 1]] - data[[i, 1]] == 0, ,
derOfData[[i, 2]] = (data[[i + 1, 2]] - data[[i, 2]])/( data[[i + 1, 1]] - data[[i, 1]]);
]
];
derOfData
```

]

This bit imports the data and puts it into a format that is easy to work with.

```
data = Import[ "C:\\filename.ods"];
data = data[[1]];
data = Sort[data, #1[[1]] < #2[[1]] &];
ListPlot[data, Joined -> True]
```

Then we take the numerical derivative:

```
dData = SymDer[data];
dData = Table[{dData[[i, 1]], Abs[dData[[i, 2]]]}, {i, 1, Length[dData]}];
ListPlot[{data, dData}, PlotRange -> {0, 10}, Joined -> True]
```

This is the best-fit code. I fitted to a Gaussian.

```
params = FindFit[dData, a Exp[-(x - b)^2/(2 c^2)], {a, b, c}, x]
Trendline[x_] = a Exp[-(x - b)^2/(2 c^2)] /. params;

Show[ListPlot[dData], Plot[Trendline[x], {x, -.2, .2}], PlotRange -> {0, 10}]
```

The axial resolution is the full width, half max of the Gaussian. This can be obtained from the "params" set.

```
FWHM = 2 Sqrt[2 Log[2]] c /. params
```

APPENDIX B - SQUID PROGRAM DETAILS

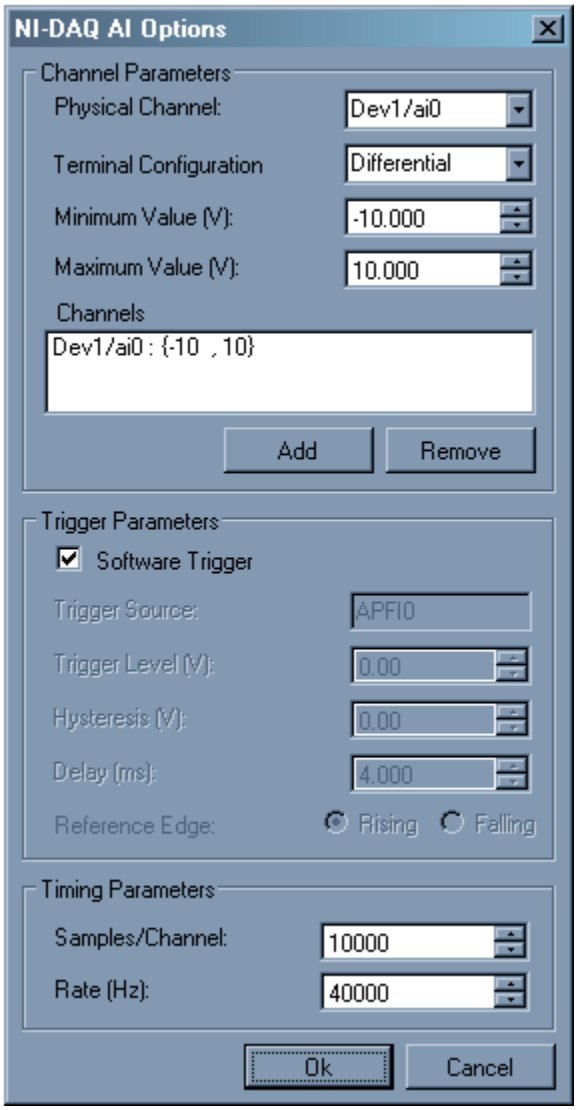

Figure B.1: These are the settings used under the "NI_DAQ Options" located in the Options tab of the SQUID Program

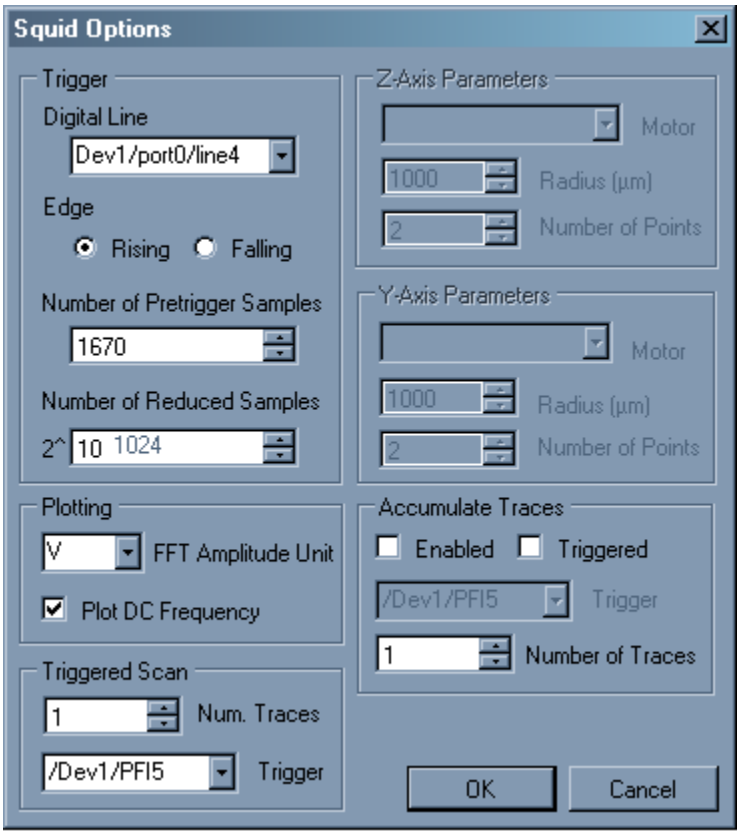

Figure B.2: This is the "SQUID Options" menu under the "Options" tab in the SQUID interface. Here you can center the signal using "Number of pretrigger samples" and can enable Accumulated Traces. If "1" is selected for the number of accumulated traces, SQUID will accumulate indefinitely.